Research Article

Structure-function analyses reveal *Arabidopsis thaliana* HDA7 to be an inactive histone deacetylase

Ketul Saharan [a,b], Somanath Baral [a], Nausad Hossain Shaikh [a], Dileep Vasudevan [a,c,*]

[a] *Structural Biology Laboratory, Institute of Life Sciences (ILS), Bhubaneswar, 751023, India*
[b] *Regional Centre for Biotechnology (RCB), Faridabad, 121001, India*
[c] *Structural Biology Laboratory, Rajiv Gandhi Centre for Biotechnology (RGCB), Thiruvananthapuram, 695014, India*

ABSTRACT

Histone deacetylases (HDACs), responsible for the removal of acetyl groups from histone tails, are important epigenetic factors. They play a critical role in the regulation of gene expression and are significant in the context of plant growth and development. The Rpd3/Hda1 family of HDACs is reported to regulate key biological processes in plants, such as stress response, seed, embryonic, and floral development. Here, we characterized *Arabidopsis thaliana* HDA7, a Class I, Rpd3/Hda1 family HDAC. SAXS and AUC results show that the recombinantly expressed and purified histone deacetylase domain of AtHDA7 exists as a monomer in solution. Further, the crystal structure showed AtHDA7 to fold into the typical α/β arginase fold, characteristic of Rpd3/Hda1 family HDACs. Sequence analysis revealed that the Asp and His residues of the catalytic 'XDXH' motif present in functional Rpd3/Hda1 family HDACs are mutated to Gly and Pro, respectively, in AtHDA7, suggesting that it might be catalytically inactive. The Asp and His residues are important for Zn^{2+}-binding. Not surprisingly, the crystal structure did not have Zn^{2+} bound in the catalytic pocket, which is essential for the HDAC activity. Further, our *in vitro* activity assay revealed AtHDA7 to be inactive as an HDAC. A search in the sequence databases suggested that homologs of AtHDA7 are found exclusively in the Brassicaceae family to which Arabidopsis belongs. It is possible that HDA7 descended from HDA6 through whole genome duplication and triplication events during evolution, as suggested in a previous phylogenetic study.

1. Introduction

The organization of the eukaryotic genome is characterized by a condensed structure known as chromatin, in which the nucleosome acts as the fundamental building block. The nucleosome consists of two copies of each core histone, specifically H2A, H2B, H3, and H4, encased by a 147 base pair double-stranded DNA (Luger et al., 2000). Despite its compact structure, the chromatin undergoes dynamic transitions between two distinct states referred to as euchromatin (an open state) and heterochromatin (a condensed state) (Hübner and Spector, 2010; Woodcock and Ghosh, 2010). These transitions play a crucial role in regulating the accessibility of genomic DNA to various regulatory complexes involved in gene expression, DNA replication, repair, and the maintenance of genomic stability (Ehrenhofer-Murray, 2004). The regulation of gene expression is significantly impacted by a range of epigenetic histone modifications, including acetylation, methylation, phosphorylation, ADP ribosylation, and biotinylation, which take place

on the amino-terminal tails of the core histone proteins (Millán-Zambrano et al., 2022). The acetylation process occurring on the ε-amino group of Lysine residues within the core histone tails has been extensively investigated and is recognized as a prominent epigenetic modification mark (Seto and Yoshida, 2014).

The acetylation of the histone tails is a reversible process facilitated by two distinct groups of enzymes. The first group, described as acetyltransferases (HATs), adds the acetyl group to the histone tails (Roth et al., 2001). Conversely, the second group, HDACs, removes these acetyl marks (Seto and Yoshida, 2014). The dynamic acetylation of the core histone tails modifies nucleosome structure, which in turn modifies overall chromatin compaction. The removal of acetyl moiety escalates the electrostatic interaction between DNA and histones, thereby promoting heterochromatin formation and, ultimately, repression of gene expression (Chen et al., 2015). HDACs have been reported to exist in all eukaryotes. The metazoan and yeast HDACs are categorized into two distinct families: Zn^{2+}-dependent Reduced potassium dependency

3/Histone deacetylase-A 1 (Rpd3/Hda1) family and the NAD-dependent Sirtuin family (Seto and Yoshida, 2014).

The structural studies illustrate that the Rpd3/Hda1 family proteins hold a distinctive α/β arginase fold, characterized by a parallel β-sheet that is flanked by α-helices on both sides of the sheet (Seto and Yoshida, 2014). The catalytic pocket accommodates a Zn^{2+} ion coordinated by catalytic residues and a water molecule to execute the nucleophilic attack on the carbonyl group to deacetylate the substrate (Lombardi et al., 2011). Multiple studies have evidenced the significant involvement of Rpd3/Hda1 HDACs in controlling gene transcription, maintaining genome stability, regulating DNA replication and repair, facilitating cell cycle progression, induction of apoptosis, and other biological processes (Krämer et al., 2001; Seto and Yoshida, 2014).

The classification of *A. thaliana* HDACs into three families, namely Rpd3/Hda1, Sirtuins, and HD-tuins, has been done based on sequence conservation with well-characterized yeast and human HDACs. Notably, the HD-tuin HDACs are restricted to plants (Chen et al., 2020) and have recently been characterized as functional nucleoplasmins (Bobde et al., 2022). The Rpd3/Hda1 family in *A. thaliana* has been further categorized into three distinct classes - Class I (HDA1/19, HDA6, HDA7, HDA9, HDA10, and HDA17), Class II (HDA5, HDA8, HDA14, HDA15, HDA18) and Class IV (HDA2) (Chen et al., 2020). Over the past decade, the genetic and functional investigations of plants have revealed that HDACs play a pivotal role in regulating various vital cellular processes in plants. The various Rpd3/Hda1 family members of *A. thaliana* have been reported to play an important role in processes such as seed germination, seed dormancy, salt tolerance, root epidermis cell patterning, circadian rhythm, flowering, embryo and leaf development (Ueda et al., 2017; Zheng et al., 2016; Liu et al., 2013; Xu et al., 2005; Gu et al., 2017; Luo et al., 2015; Hung et al., 2018; Wang et al., 2013; Gao et al., 2015; Tanaka et al., 2008; Van Zanten et al., 2014). The repression of AtHDA7 has been seen to diminish seed and ovule development (Cigliano et al., 2013). Knockout (KO) studies revealed that the plant class I Rpd3/Hda1 HDACs display specificity towards H3 histone for targeting the acetyl-lysine. For instance, HDA5 KO resulted in increased acetylation at H3K9 and H3K14 (Luo et al., 2015); HDA1/19 KO enhanced H3K9 acetylation (Zhou et al., 2010); HDA9 KO enhanced the H3K9 and H3K27 acetylation (Kim et al., 2016). Furthermore, Arabidopsis HDACs have been reported to target certain non-histone proteins for deacetylation (Hartl et al., 2017; Hao et al., 2016; Tran et al., 2012).

The Rpd3/Hda1 HDACs have been extensively structurally and functionally characterized in human and yeast to explore their therapeutic importance (Krämer et al., 2001). However, only one Class II Rpd3/Hda1 family member from plants, *A. thaliana* HDA15, has been structurally and functionally explored so far (Chen et al., 2020). Here, we present the structural and functional characterization of *A. thaliana* HDA7 belonging to Class I Rpd3/Hda1 HDAC. Biophysical studies showed that the recombinantly expressed AtHDA7 is a homogenous monomer. Our crystal structure and activity assay results revealed that AtHDA7 is an inactive HDAC. However, in the absence of an HDAC activity, it is not clear how the repression of AtHDA7 will affect seed and ovule development, as reported previously.

2. Material and Methods

2.1. Multiple sequence alignment

The multiple sequence alignments of AtHDA7 with other *A. thaliana* Rpd3/Hda1 HDACs and human class I Rpd3/Hda1 HDACs were performed using the T-coffee server (Di Tommaso et al., 2011) and the Esprit 4.0 server (Robert and Gouet, 2014) was utilized for preparing pictorial representations.

2.2. Cloning, expression, and purification

A. thaliana HDA7 HD (spanning residues 5 to 383) was prepared using the codon-optimized genes obtained from GenScript (Supp. Figs. 1A and 1B). AtHDA7 HD ORF was amplified by a set of DNA oligos using PCR (Supp. Fig. 1C). After digestion, the amplified products were ligated into a pET22b(+) vector using *Nde*I and *Xho*I restriction endonucleases. The ligation product was transformed into *E. coli* DH5α strain cells and plated on LB ampicillin plates, and the clones were validated by colony PCR and DNA sequencing.

The confirmed plasmid having AtHDA7 HD was transformed into *E. coli* BL21 (DE3) GroEL strain cells were plated on LB agar plates supplemented with ampicillin (100 μg/ml) and chloramphenicol (25 μg/ml) antibiotics. A single colony from the transformed plate was inoculated into 5 ml 2xYT medium with ampicillin (100 μg/ml) and chloramphenicol (25 μg/ml) and grown overnight at 37 °C at 220 rpm in a shaker incubator. This overnight culture was sub-cultured into 1 L of fresh 2xYT broth with ampicillin (100 μg/ml) and chloramphenicol (25 μg/ml) and induced with 0.2 g/l arabinose at OD_{600} of 0.4, followed by 0.3 mM IPTG at OD_{600} of 0.6 and grown for 18 h at 16 °C at 220 rpm in a shaker incubator.

The cells were harvested by centrifugation and resuspended in 50 ml lysis buffer containing 20 mM Tris-HCl (pH 7.5), 500 mM NaCl, 5% glycerol, 10 mM arginine, 1 mM β-mercaptoethanol, 20 mM Imidazole (pH 7.5), and one EDTA-free protease inhibitor cocktail tablet (Roche) and lysis was performed using a Vibra-Cell probe-type ultrasonic processor (Sonics). The lysate was centrifuged at 18,000 rpm for 1 h at 4 °C, and the supernatant was loaded onto a HisTrap FF 5 ml nickel affinity column (Cytiva) pre-equilibrated with lysis buffer. The AtHDA7 HD was co-expressed with the GroEL chaperone to enhance its folding and solubility, which otherwise was found in the insoluble fraction after the bacterial cell lysis. However, upon analysis, the GroEL chaperone was found strongly bound and was getting co-purified with AtHDA7 HD. The affinity chromatography column was washed with three column volumes of the lysis buffer containing 1 mM ATP, which helped remove the GroEL chaperone. Further, the affinity column was washed 10 column volume with wash buffer containing 20 mM Tris-HCl (pH 7.5), 300 mM NaCl, 5% glycerol, 10 mM arginine, 1 mM β-mercaptoethanol, 50 mM Imidazole (pH 7.5). Finally, the bound protein was eluted from the column with elution buffer containing 20 mM Tris-HCl (pH 7.5), 300 mM NaCl, 5% glycerol, 10 mM arginine, 1 mM β-mercaptoethanol, 300 mM Imidazole (pH 7.5). The eluted AtHDA7 HD was further subjected to size-exclusion chromatography using a HiLoad 16/600 Superdex 75 prep grade column (Cytiva) pre-equilibrated in SEC buffer containing 20 mM Tris-HCl (pH 7.5), 150 mM NaCl and 1 mM β-mercaptoethanol. The purification steps were performed using an AKTA Pure 25M system maintained at 4 °C. The purified AtHDA7 HD was concentrated using a 30 KDa Vivaspin Turbo centrifugal concentrator (Sartorius) to 7 mg/ml for further experiments.

2.3. Analytical ultracentrifugation

The sedimentation velocity analytical ultracentrifugation (SV-AUC) experiment for AtHDA7 HD was performed using an Optima AUC analytical ultracentrifuge (Beckman Coulter). The SEC-purified AtHDA7 HD was diluted to an OD_{280} value of 0.6 before being subjected to AUC. The AtHDA7 HD samples were centrifuged at 40,000 rpm and 20 °C temperature in an AN-60 Ti rotor, and the absorbance scans at 280 nm were collected for 20 h at 90-s frequency intervals. For data analysis, SEDNTERP and SEDFIT software were employed. SEDNTERP was utilized to estimate the density and viscosity of the buffer and the partial specific volume of the protein (Philo, 2023). SEDFIT was used to process the raw absorbance data employing the continuous size distribution model (Zhao et al., 2013). The graphs for the analysis were prepared using GUSSI (Zhao et al., 2013).

2.4. Small-angle X-ray scattering (SAXS)

The SAXS experiments for the AtHDA7 HD were conducted at the

BM29 BioSAXS beamline of the European Synchrotron Radiation Facility (ESRF, Grenoble, France). The ATSAS PRIMUS suit was employed for averaging, subtraction, data analysis, and obtaining various parameters (Franke et al., 2017). DAMMIF was utilized to prepare the bead model from the experimental SAXS data. The experimental scattering from SAXS was compared with the AtHDA7 HD crystal structure using the FoXS server (Schneidman-Duhovny et al., 2016). The SAXS envelope structure figures were prepared using PyMOL (Schrödinger, LLC).

2.5. Crystallization, data collection, and data processing

The recombinantly expressed and purified AtHDA7 HD at a concentration of 7 mg/ml was subjected to crystallization screening using different commercial screening kits at 18 °C in 96-well MRC plates with the help of a Mosquito Xtal3 crystallization robot (SPT Labtech). Crystals obtained from the screening solutions were optimized in 24-well hanging drop plates at 18 °C. A thick prism-shaped crystal from a solution having 0.1 M HEPES (pH 7.5) and 25% PEG 3350 was used for data collection. Before data collection, the crystal was soaked in the crystallization solution supplemented with 20% PEG 400 as a cryoprotectant and flash-cooled in liquid nitrogen. The X-ray diffraction data for AtHDA7 HD crystal was collected at the beamline ID30-A3 of ESRF (Grenoble, France) equipped with an Eiger X 4M detector. The integration of diffracted data was performed using iMosflm software, followed by scaling and merging using Aimless software from the CCP4 suite (Winn et al., 2011). The crystal belonged to the monoclinic space group of P 1 2₁ 1. The molecular replacement method was utilized to determine the phases for the AtHDA7 HD crystal structure, employing the Phenix phaser molecular replacement program (Adams et al., 2002). HsHDA8 crystal structure (PDB ID: 1W22) was used as the search model for molecular replacement. Phenix.Refine and Coot were employed to refine the AtHDA7 HD crystal structure (Afonine et al., 2012). The representative crystal structure figures were prepared using the PyMOL visualization software (Schrödinger, LLC).

2.6. In-vitro histone deacetylase activity assay

In-vitro histone deacetylase activity assay was performed using a fluorimetric HDAC activity assay kit (Sigma, catalog number CS1010) containing a fluorogenic HDAC substrate Boc-Lys(Ac)-AMC to examine the histone deacetylase activity of AtHDA7 HD. Since AtHDA7 belongs to the class I family of HDACs and the Boc-Lys(Ac)-AMC fluorogenic substrate is more specifically identified by class I HDACs, this substrate was used for the activity assay. The assay buffer was mixed with 81 μM, 162 μM and 324 μM of AtHDA7 HD separately, followed by mixing with 50 μl of 200 mM fluorogenic HDAC substrate solution in a clear, flat bottom, black 96-well assay plate. Similarly, AtHDA18 HD as a positive control, at concentrations of 81 μM, 162 μM, and 324 μM, was mixed with assay buffer and substrate. Three separate reactions for substrate solution mixed with assay buffer were used as negative control. The reactions were then incubated for 30 min at 30 °C, followed by adding 10 μl developer solution and further incubated for 20 min at room
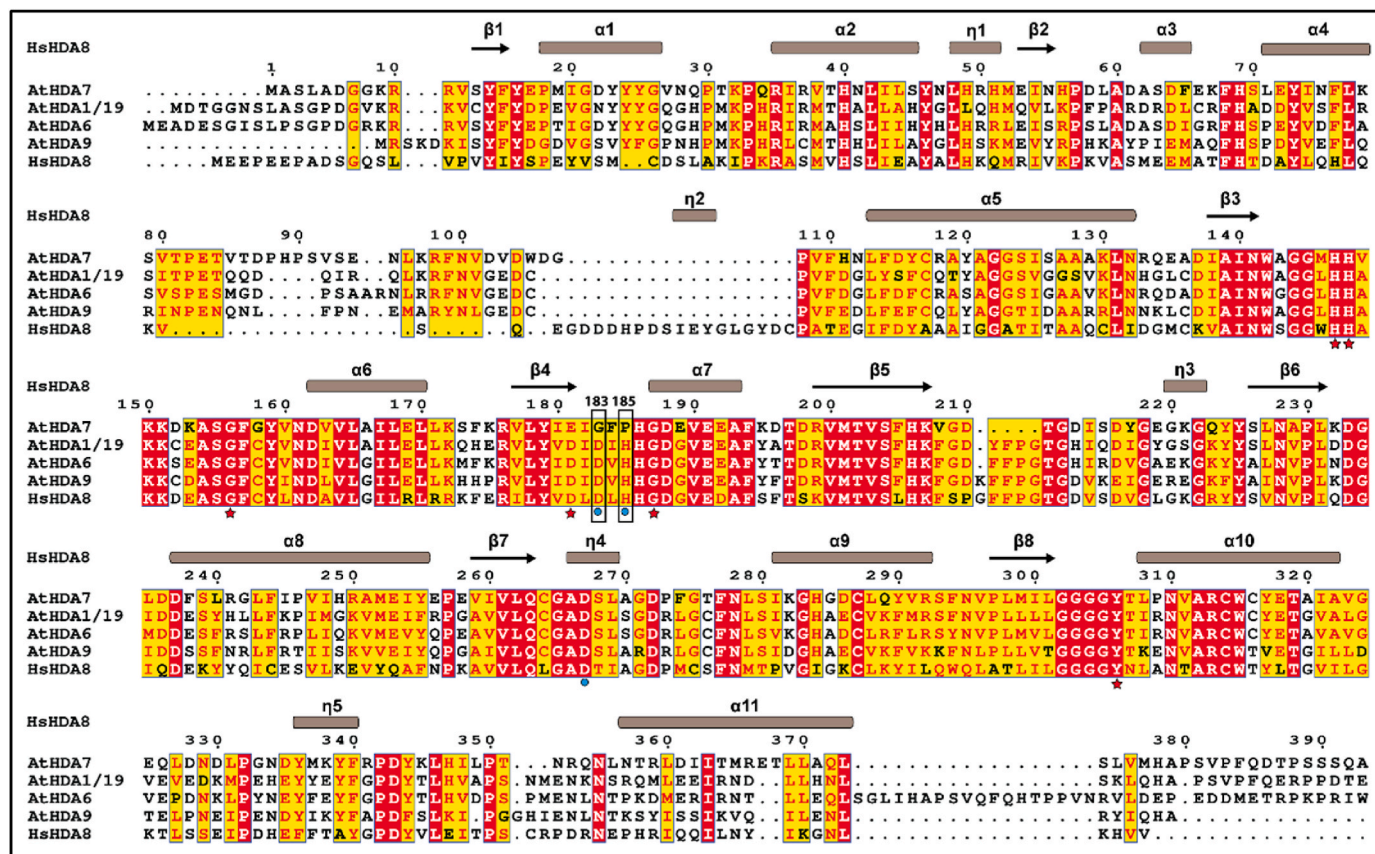
Fig. 1. Multiple sequence alignment of AtHDA7 with human class I **Rpd3/Hda1** HDACs. The multiple sequence alignment of *A. thaliana* HDAC7 with class I Rpd3/Hda1 HDACs, including AtHDA1/19, AtHDA6, AtHDA9 and HsHDA8. The yellow boxes show similar residues, while the red boxes show identical residues. The red-colored star symbols illustrate the catalytic residues involved in substrate binding, while the cyan-colored circles show the residues involved in zinc binding. The residue numbering is shown for AtHDA7 while the secondary structural illustrations (α is α-helix, β is β-strand, and η is 3¹⁰-helix) are shown for the HsHDA8. The residues substituted in the case of AtHDA7 are shown in the black boxes with residue numbering. The multiple sequence alignment was performed using the T-coffee server, and its pictorial representation was constructed using the Esprit 4.0 server. (For interpretation of the references to color in this figure legend, the reader is referred to the Web version of this article.)

temperature. Finally, the fluorescence intensity of reactions was measured using a Varioskan multi-plate reader (Thermo Fisher) at an excitation wavelength of 350 nm and an emission wavelength of 460 nm. Each reaction was performed in triplicate.

3. Results

3.1. Sequence alignment of AtHDA7 with other class I Rpd3/Hda1 HDACs

The sequence conservation of AtHDA7 (Uniprot ID Q9FH09) was examined using sequence alignment with human and *A. thaliana* Rpd3/Hda1 family members (Fig. 1 & Supp. Fig. 2). Sequence alignment with Rpd3/Hda1 members from human and *A. thaliana* revealed over ~40% and ~50% identity, respectively, with conserved substrate binding residues in the catalytic pocket. However, interestingly, sequence alignment revealed that unlike other human and *A. thaliana* Rpd3/Hda1 HDACs, in AtHDA7, the Asp and His residues of the catalytic pocket from the 'XDXH' motif essential for coordination with Zn^{2+} are replaced by Gly and Pro residues to form an 'XGXP' motif. This observation indicated that AtHDA7 could be catalytically inactive.

3.2. Recombinant expression and purification of AtHDA7 HD

The histone deacetylase domain of AtHDA7 full-length (FL) protein is flanked by a few residues at both N and C-terminus with considerable flexibility (Fig. 2A). Therefore, the open reading frame coding for AtHDA7 containing only the histone deacetylase domain (HD; residues 5–383) was cloned and expressed. This construct yielded the protein in the soluble fraction. Further, affinity chromatography followed by size-exclusion chromatographic (SEC) purification gave a homogenous peak for AtHDA7 HD at 66 ml (Fig. 2B). The SDS-PAGE analysis of AtHDA7 HD SEC elution gave an intense band at 43 kDa corresponding to its theoretical molecular weight (Fig. 2C).

3.3. In-solution oligomeric status of AtHDA7 HD

Sedimentation velocity-analytical ultracentrifugation (SV-AUC) and small angle X-ray scattering (SAXS) were used to understand the in-solution oligomeric state and to obtain a low-resolution envelope structure of AtHDA7 HD. The SV-AUC of the SEC purified protein

resulted in a sedimentation coefficient value of 3.45 S and a molecular weight value of 43.67 kDa, which corroborated well with the theoretical molecular weight of its monomer (Fig. 3). The peak corresponding to 43 kDa gave over 85% distribution of the total protein, suggesting that the protein was homogenous and pure (Table 1). The SV-AUC results suggested that the AtHDA7 HD is monomeric in solution.

The SAXS experiment was conducted at the BM29 BioSAXS beamline of ESRF, Grenoble. The data collection and data processing parameters are shown in Table 2. The Guinier profile of the scattering suggested that the sample is free of potential aggregation (Fig. 4A). The Kratky plot gave a Gaussian distribution, which, however, approached a higher value toward the end of the X-axis, suggesting the protein is globular but has some flexibility, probably contributed by the C-terminal hexa-histidine tag (Fig. 4B). The distance distribution plot gave a Dmax value of 10.16 nm (Fig. 4C). The estimation of molecular weight using the Porod volume (*Vp/1.7*) yielded a value of 51.59 kDa, which appeared close to the theoretical molecular weight. The averaged beaded envelope generated using DAMAVAR demonstrated a globular shape with a partial protrusion at one end. The structure model fitted well with the beaded envelope while accommodating the C-terminal hexa-histidine tag at the protruding end of the envelope (Fig. 4D). Furthermore, the analysis of experimental scattering from the sample versus theoretical scattering from the structure model yielded reasonably acceptable goodness of fit (Chi-square 'χ^2') value of 2.48 (Fig. 4E). The SAXS results revealed that AtHDA7 HD is monomeric, with the C-terminal tag providing an elongated shape, agreeing well with the AUC results.

3.4. Crystal structure of AtHDA7 HD

A crystallization condition having 25% PEG3350 and 50 mM HEPES (pH 7.5) yielded a few prism-shaped crystals for AtHDA7 HD. One of them diffracted to a resolution of 1.5 Å. The crystal belonged to the monoclinic space group of $P2_1$, with unit cell dimensions of a = 47.31 Å, b = 74.37 Å, c = 47.59 Å, α = 90° β = 112.2° and γ = 90°. Matthew's coefficient suggested a single subunit of AtHDA7 HD in the asymmetric unit. The crystal structure was solved by molecular replacement method utilizing the structure coordinates of HsHDAC8 (PDB ID: 1W22) as the search model. The data collection and refinement statistics are given in Table 3. AtHDA7 HD structure comprises eight parallel β-strands, fifteen α-helices, and three 3_{10} helices (Fig. 5A and B). The overall structure
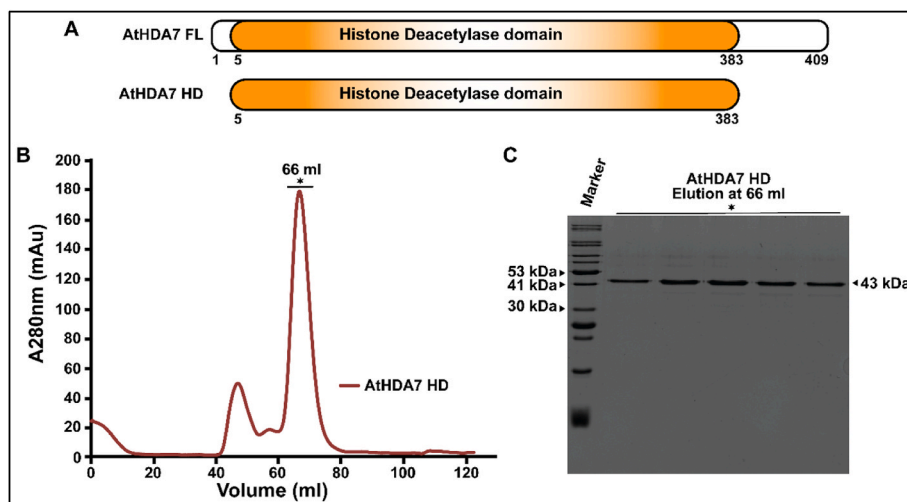
Fig. 2. Construct design and purification of AtHDA7 HD. (A) Illustration of AtHDA7 construct design. The full-length AtHDA7 possesses a central histone deacetylase domain (in orange) flanked by a few residues at both ends that are relatively disordered and hence avoided in the construct design. (B) The size-exclusion chromatographic purification profile of AtHDA7 HD shows a major peak at 66 ml and a minor peak near 50 ml. (C) The SDS-PAGE analysis of eluted fraction from the major peak gave a single band of 43 kDa, which is equivalent to the theoretical molecular weight of AtHDA7 HD. The asterisk symbol shows the elution fractions from SEC loaded on the SDS-PAGE. (For interpretation of the references to color in this figure legend, the reader is referred to the Web version of this article.)
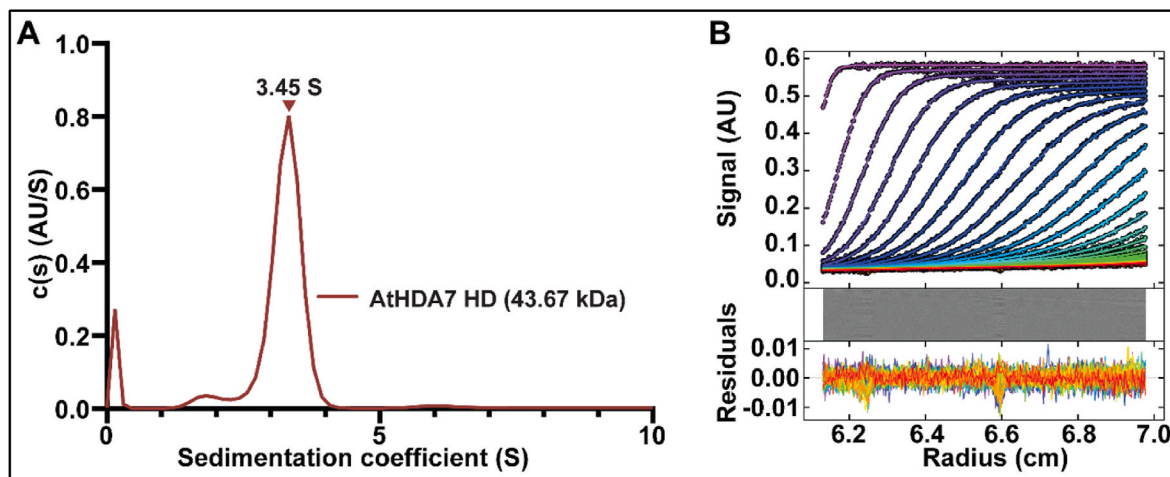
Fig. 3. Sedimentation velocity analytical ultracentrifugation analysis of AtHDA7 HD. (A) SV-AUC of AtHDA7 HD illustrating the continuous distribution as a function of sedimentation coefficient profile. AtHDA7 HD sample demonstrated a major peak with over 85% distribution, suggesting the protein adopts a monomeric state. (B) The upper panel shows the representative progressive absorbance scans fitted using the continuous distribution model. The middle and lower panel shows the bitmap and the residual plot.

Table 1
Sedimentation velocity - analytical ultracentrifugation (SV-AUC) data for AtHDA7 HD.

Protein Identity	Sedimentation Coefficient (S)	Population distribution (%)	Calculated Molecular mass (kDa)	Frictional Ratio (f/fo)	Stokes Radius (nm)	RMSD
AtHDA7 HD	3.45	85.75	43.67	1.29	3.02	0.002

Table 2
SAXS data collection and structure parameters.

	AtHDA7 HD
Data collection parameter	
Beamline	BM29 BioSAXS (ESRF)
Wavelength (Å)	0.9794
Energy (KeV)	7–15
Detector	Pilatus3 2M
Q range (nm^{-1})	0.025–6
Beam size at sample (μm^2)	200×200
Concentration (mg/ml)	1.0
Sample to detector distance (m)	2.867
Absolute intensity calibration	Water
Sample volume	50 µl
Temperature	20 °C
Structural parameters	
Rg (Å) (from $P(r)$)	2.99 ± 0.06
$I(0)$ (cm^{-1}) (from $P(r)$)	67.13 ± 0.31
Rg (Å) (from Guinier)	2.97 ± 0.02
$I(0)$ (cm^{-1}) (from Guinier)	67.12 ± 0.60
Dmax (Å)	10.16
Porod volume ($Å^3$)	84718
Molecular mass determination	
From Porod volume (Vp/1.7) (kDa)	51.59
Calculated from sequence (kDa)	43.00
Chi^2	2.48
Modeling parameters	
Symmetry	P1
DAMAVER (10 DAMMIF) mean NSD*	0.584 ± 0.048
Software employed	
Primary data reduction	Beamline Pipeline
Data processing	PRIMUS
Ab-initio analysis	DAMMIF
Validation and averaging	DAMAVER
Computation of model scattering	FoXS
3D graphic model representation	PyMOL

revealed that AtHDA7 HD adopts an α/β arginase fold having a β-sheet sandwiched between α-helices, typical of an Rpd3/Hda1 HDAC.

The structure of AtHDA7 HD aligned well with human class I Rpd3/

Hda1 HDACs, including HsHDAC1, HsHDAC2, HsHDAC3, and HsHDAC8 (Fig. 5C & Table 4). However, a few minor differences were observed for the AtHDA7 HD structure compared to other Rpd3/Hda1 crystal structures. The α1-α2 loop and α6 and α7 helices of AtHDA7 HD displayed a major deviation compared to the other structures (Supp. Figs. 3A and 3B). Furthermore, the β3-α9 loop for AtHDA7 HD displayed an outward displacement of 4.2 Å. (Supp. Fig. 3C).

The crystal structure of AtHDA7 HD showed that the Asp and His residues of the 'XDXH' motif in the catalytic pocket that are essential for zinc binding in Rpd3/Hda1 HDACs are replaced by Gly and Pro residues, respectively. As such, a Zn^{2+} ion was not present in the structure, as evidenced by the lack of electron density (Fig. 6A, Supp. Fig. 4). Whereas the previously studied crystal structures of class I Rpd3/Hda1 HDACs members, including HsHDAC1 (PDB ID:4BKX), HsHDAC2 (PDB ID:7ZZO), HsHDAC3 (PDB ID:4A69) and HsHDAC8 (PDB ID:1W22), displayed conserved Asp and His residues of the 'XDXH' motif coordinating with the Zn^{2+} ion, along with another Asp residue (Fig. 6B–E). Since the Zn^{2+} ion is essential for the deacetylation activity by facilitating the nucleophilic attack on the acetylated substrate, the crystal structure indicated that AtHDA7 HD could be an inactive HDAC.

3.5. Histone deacetylase activity of AtHDA7 HD

To investigate the catalytic activity of AtHDA7 HD, an *in vitro* histone deacetylase activity assay was performed. The *Arabidopsis thaliana* HDA18 domain (AtHDA18 HD), an RPD3 class II histone deacetylase (Supp. Fig. 5 and Supp. Material and Methods), was used as a positive control. BSA was used as a negative control while assessing the histone deacetylase activity. Increasing concentrations of AtHDA7 HD displayed RFU values close to zero, confirming that it has no histone deacetylation activity. On the other hand, AtHDA18 HD displayed positive RFU values (Fig. 7). This observation is supported by the absence of Zn^{2+} ions and the Asp and His residues of the 'XDXH' motif in the crystal structure.
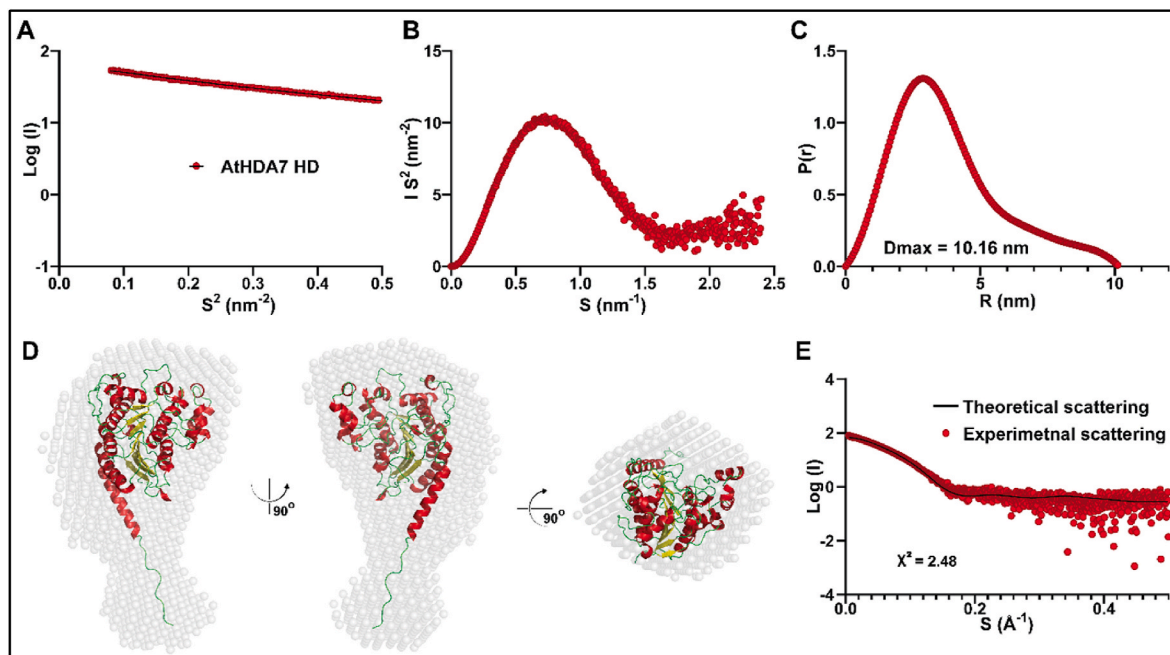
Fig. 4. Small angle X-ray scattering analysis of AtHDA7 HD. (A) The straight-line fitting to the data point in the Guinier plot indicates that the protein sample has no aggregation. (B) The Kratky plot with the partial bell-shaped distribution demonstrates that the AtHDA7 HD has marginal flexibility. (C) The distance distribution profile indicates that the protein is partially extended in nature with a Dmax value of 10.16 nm. (D) The SAXS-derived low-resolution beaded envelope (in grey) fitted with the AtHDA7 HD crystal structure (helix in red, strands in yellow, unstructured region in green) with a C-terminal hexa-histidine tag added. (E) The plot shows the overlapped profile of experimental scattering from SAXS and theoretical scattering from the AtHDA7 HD crystal structure. A χ^2 value of 2.48 shows that the experimental and theoretical scattering aligns well. (For interpretation of the references to color in this figure legend, the reader is referred to the Web version of this article.)

Table 3

X-ray diffraction data collection, processing, and structure refinement parameters.

| Parameters	AtHDA7 HD
Data collection and processing	
Beamline	ID30-A3
Detector type	Eiger X 4M
Wavelength (Å)	0.8731
Data collection temperature	100 K
Space group	$P2_1$
a, b, c (Å)	47.31, 74.37, 47.59
α, β, γ (°)	90, 112.02, 90
Resolution (Å)	43.86–1.50
R_{merge} (%)	0.336 (1.814)
I/σI	9.7 (3.2)
Refinement	
CC (1/2) (%)	0.93 (0.703)
Total no. of reflections	47979 (2387)
Completeness (%)	98.1 (96.8)
Multiplicity	7.9 (7.2)
Wilson B-factor (Å^2)	13.5
Solvent content (%)	43.0
No. of molecules in ASU	1
R_{work}/R_{free} (%)	16.1/20.2
Total no. of non-H atoms	2968
No. of water molecules	184
Mean B-factor (Å^2)	16.0
Molprobity score	1.25
Clash score	0.86
R.M.S. Deviations:	
Bond lengths (Å)	0.009
Bond angles (°)	1.56
Ramachandran plot values (%):	
Favored/Allowed/Outliers	98.66/1.34/0.00
Rotamer outliers	0.32

The values in parentheses are for the outermost shell.

4. Discussion

Histone deacetylases (HDACs) are important epigenetic factors that regulate gene expression (Seto and Yoshida, 2014). In plants, HDACs are involved in essential developmental processes, including embryonic and seed development, flowering, stress response, and maintenance of stem cells (Ma et al., 2013; Chen et al., 2020). Despite notable progress, our understanding of the structural aspects of plant HDACs remains sparse. Structural understanding is essential to comprehend the mechanistic insights of HDACs and their interactions with transcription regulatory complexes. In this context, we investigated the structural and functional insights of *A. thaliana* HDAC, HDA7.

Studies demonstrate that the Rpd3/Hda1 class of HDACs have a shared evolutionary origin with arginases and acetylpolyamine amido-hydrolases, as they all trace back to a single metalloenzyme ancestor (Dowling et al., 2008). Despite their divergence, these proteins share a similar α/β arginase fold and exhibit a high degree of conservation, especially in the catalytic pocket (Dowling et al., 2008). This pocket contains conserved Asp and His residues in the form of an 'XDXH' motif and an additional Asp residue that coordinates with the metal ions necessary for the catalytic activity. The catalytic pocket of Rpd3/Hda1 HDACs coordinates a Zn^{2+} ion (Lombardi et al., 2011). Our sequence analysis of the *A. thaliana* HDA7 revealed that the Asp and His residues of the 'XDXH' motif are mutated to Gly and Pro residues, contrasting with the functional Rpd3/Hda1 HDACs. A mutational study on HsHDAC1 has revealed that a substitution of Asp176 of the 'XDXH' motif resulted in loss of catalytic activity, suggesting that this motif is essential for the deacetylation activity of HDAC1 (Hassig et al., 1998). Our crystallographic analyses revealed that the substitution of Asp and His residues of this 'XDXH' motif with Gly and Pro residues in AtHDA7 resulted in an inability of its catalytic pocket to accommodate the Zn^{2+} ion, suggesting that AtHDA7 could be catalytically inactive, which was further confirmed by an activity assay.

HsHDAC8 showed head-to-head arranged dimers in its crystal
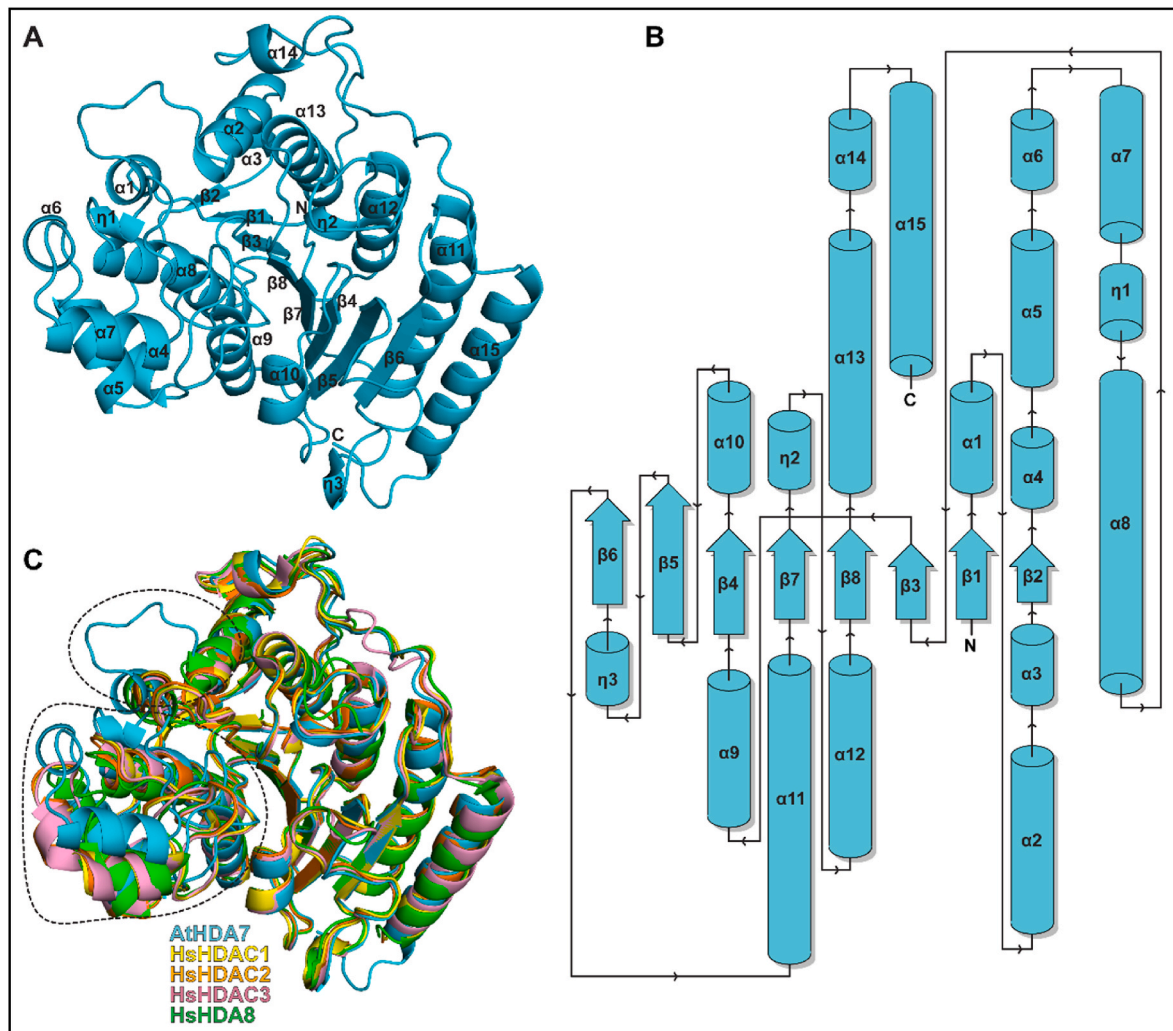
Fig. 5. Crystal structure of AtHDA7 HD and comparison with other Class I Rpd3/Hda1 crystal structures. (A) The crystal structure of AtHDA7 HD (cyan) is shown in the cartoon model. The α/β arginase fold of AtHDA7 HD holds α-helices (α1 to α15), 3_{10} helices (η1 to η 3) and parallel β-strands (β1 to β8). (B) The 2D topology diagram of AtHDA7 HD. The α-helix (α), 3_{10}-helix (η), and the β-strands are in cyan. **(C)** The structural alignment of AtHDA7 HD with human Class I Rpd3/Hda1 HDACs, wherein AtHDA7 HD is in cyan, HsHDAC1 is in yellow (PDB ID: 4BKX), HsHDAC2 is in orange (PDB ID: 7ZZO), HsHDAC3 is in pink (PDB ID: 4A69) and HsHDAC8 in green (PDB ID: 1W22). The regions within the black-dotted area show major variations among the aligned structures. (For interpretation of the references to color in this figure legend, the reader is referred to the Web version of this article.)

Table 4
Structural comparison statistics of AtHDA7 HD versus other class I Rpd3/Hda1 HDACs.

Class I Rpd3/Hda1 HDACs	PDB IDs	RMSD (Å)	No. of Cα atoms
HsHDAC1	4BKX	0.888	290
HsHDAC2	7ZZO	0.688	286
HsHDAC3	4A69	0.796	287
HsHDAC8	1W22	1.056	271

packing; however, its oligomeric state in solution was monomeric (Vannini et al., 2004). Analytical-SEC experiments showed that the AtHDA15 domain exists as a monomer and tetramer, with the tetrameric form exhibiting greater activity than the monomeric state (Chen et al., 2020). The presence of monomeric forms of AtHDA5 HD and AtHDA18 HD was also observed, and these forms were found to have catalytic activity (Chen et al., 2020). Our AUC and SAXS results implied that the AtHDA7 HD adopts a monomeric form in solution. The *in vitro* activity assay revealed that the AtHDA7 HD is catalytically inactive, consistent with the sequence and structural analyses.

In summary, here we present the first structural and functional

characterization of an inherently inactive HDAC, AtHDA7, primarily due to residue substitutions necessary for Zn^{2+} ion coordination in the catalytic pocket. Moreover, a database search with the AtHDA7 sequence demonstrated that its homologs, with substitutions for the Asp and His residues of the 'XDXH' motif, are found exclusively among members of the Arabidopsis, Brassica, Raphanus, and Capsella genera (Supp. Fig. 6), belonging to the Brassicaceae family. A recent phylogenetic investigation has revealed that, in Arabidopsis and Brassica, HDA7 might have originated from HDA6, another member of the class I Rpd3/Hda1 HDAC family, possibly owing to multiple whole genome duplication and triplication events during evolution (Yruela et al., 2021). However, despite the catalytic inactivity, previous research has demonstrated that the deletion of AtHDA7 results in hyperacetylation, diminished seed formation, female gametophyte development, and embryonic development (Cigliano et al., 2013). Plant HDACs have been shown in previous studies to interact with different regulatory complexes and other HDACs. For example, the interaction of maize HDA6 with HD2 HDAC was discovered to be critical in the development of salt stress tolerance (Luo et al., 2012). Likewise, we hypothesize that AtHDA7 might function as a critical subunit in multiprotein regulatory complexes, and deletion of AtHDA7 probably results in the inability to
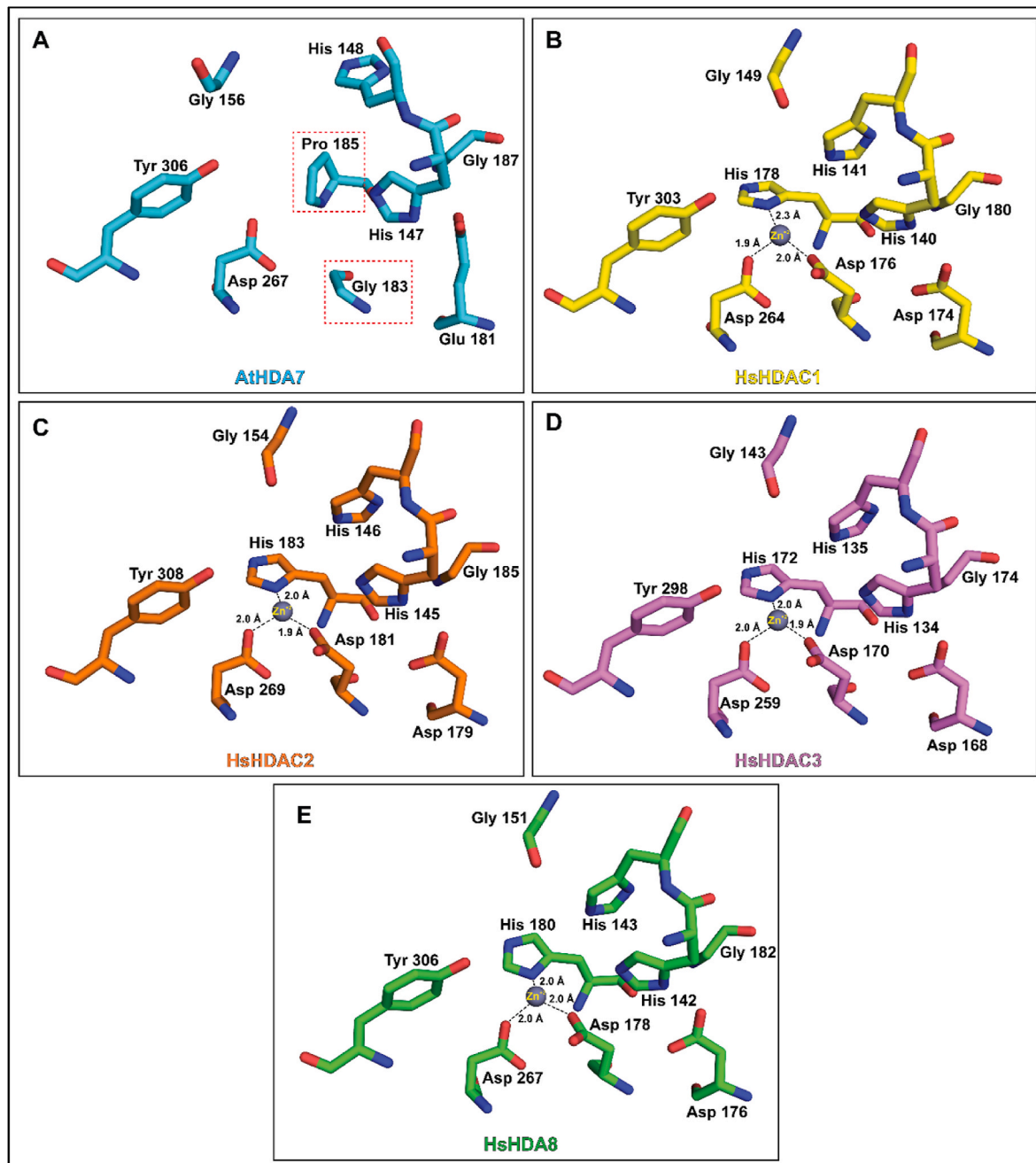
Fig. 6. Structural comparison of the catalytic pocket residues of AtHDA7 with other Class I Rpd3/Hda1 HDAC crystal structures. The residues responsible for deacetylase activity in the catalytic pocket are illustrated as sticks for **(A)** AtHDA7 (cyan), **(B)** HsHDAC1 (PDB ID: 4BKX) (yellow), **(C)** HsHDAC2 (PDB ID: 7ZZO) (orange), **(D)** HsHDAC3 (PDB ID: 4A69) (pink) and **(E)** HsHDAC8 (PDB ID: 1W22) (green). The Zn^{2+} ion is shown as a grey sphere. The black dotted lines represent the coordination of Zn^{2+} ion with catalytic residues. The red dotted boxes in **(A)** highlight the Gly183 and Pro185 residues in the catalytic pocket of AtHDA7. (For interpretation of the references to color in this figure legend, the reader is referred to the Web version of this article.)

form such complexes, thus leading to developmental abnormalities. However, this needs to be experimentally explored, and the interaction partners for AtHDA7 need to be identified to further our understanding of the significance of AtHDA7 in the plant development context.
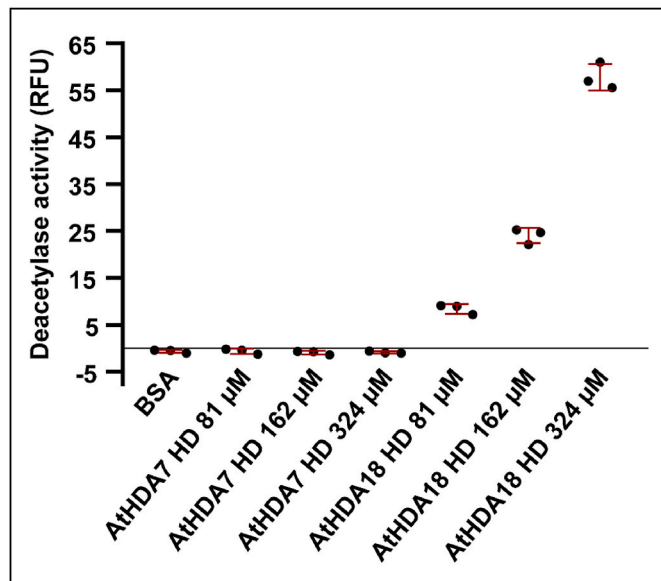
Accession number

Atomic coordinates and structure factor of AtHDA7 HD crystal structure have been deposited with the PDB accession ID 8WZL. SAXS data of AtHDA7 HD has been deposited in the SASBDB database with accession ID SASDUK2.

Fig. 7. *In vitro* **histone deacetylase activity assay of AtHDA7 HD.** The graph displays the histone deacetylase activity as a relative fluorescence unit (RFU). AtHDA7 HD at three increasing concentrations did not display deacetylase activity, similar to BSA (negative control). AtHDA18 HD at three increasing concentrations served as positive control and demonstrated deacetylase activity. The Error bars (dark red) in the graph demonstrate the standard deviation (SD) of three technical replicates. The black dots represent the RFU values of three replicates for respective samples. (For interpretation of the references to color in this figure legend, the reader is referred to the Web version of this article.)

CRediT authorship contribution statement

Ketul Saharan: designed and carried out all the experiments, analyzed data, and wrote the manuscript. **Somanath Baral:** assisted in the cloning, expression, and purification work. **Nausad Hossain Shaikh:** assisted in the crystallization work. **Dileep Vasudevan:** designed the experiments, obtained funding, analyzed data, and wrote the manuscript.

Declaration of competing interest

The authors declare that they have no known competing financial interests or personal relationships that could have appeared to influence the work reported in this paper.

Data availability

Data will be made available on request.

Acknowledgment

Appendix A. Supplementary data

Supplementary data to this article can be found online at https://doi.org/10.1016/j.crstbi.2024.100136.

References

Adams, P.D., Grosse-Kunstleve, R.W., Hung, L.W., Ioerger, T.R., McCoy, A.J., Moriarty, N.W., Read, R.J., Sacchettini, J.C., Sauter, N.K., Terwilliger, T.C., 2002. PHENIX: building new software for automated crystallographic structure determination. Acta Crystallogr D Biol Crystallogr 58 (Pt 11), 1948–1954. https://doi.org/10.1107/s0907444902016657.

Afonine, P.V., Grosse-Kunstleve, R.W., Echols, N., Headd, J.J., Moriarty, N.W., Mustyakimov, M., Terwilliger, T.C., Urzhumtsev, A., Zwart, P.H., Adams, P.D., 2012. Towards automated crystallographic structure refinement with phenix.refine. Acta Crystallogr D Biol Crystallogr 68 (Pt 4), 352–367. https://doi.org/10.1107/S0907444912001308.

Bobde, R.C., Kumar, A., Vasudevan, D., 2022. Plant-specific HDT family histone deacetylases are nucleoplasmins. Plant Cell 34 (12), 4760–4777. https://doi.org/10.1093/plcell/koac275.

Chen, C.Y., Tu, Y.T., Hsu, J.C., Hung, H.C., Liu, T.C., Lee, Y.H., Chou, C.C., Cheng, Y.S., Wu, K., 2020. Structure of Arabidopsis HISTONE DEACETYLASE15. Plant Physiol 184 (3), 1585–1600. https://doi.org/10.1104/pp.20.00604.

Chen, H.P., Zhao, Y.T., Zhao, T.C., 2015. Histone deacetylases and mechanisms of regulation of gene expression. Crit. Rev. Oncog. 20 (1-2), 35–47. https://doi.org/10.1615/critrevoncog.2015012997.

Chen, X., Ding, A.B., Zhong, X., 2020. Functions and mechanisms of plant histone deacetylases. Sci. China Life Sci. 63 (2), 206–216. https://doi.org/10.1007/s11427-019-1587-x.

Cigliano, R.A., Cremona, G., Paparo, R., Termolino, P., Perrella, G., Gutzat, R., Consiglio, M.F., Conicella, C., 2013. Histone deacetylase AtHDA7 is required for female gametophyte and embryo development in Arabidopsis. Plant Physiol 163 (1), 431–440. https://doi.org/10.1104/pp.113.221713.

Di Tommaso, P., Moretti, S., Xenarios, I., Orobitg, M., Montanyola, A., Chang, J.M., Taly, J.F., Notredame, C., 2011. T-Coffee: a web server for the multiple sequence alignment of protein and RNA sequences using structural information and homology extension. Nucleic Acids Res. 39 https://doi.org/10.1093/nar/gkr245 (Web Server issue): W13-7.

Dowling, D.P., Di Costanzo, L., Gennadios, H.A., Christianson, D.W., 2008. Evolution of the arginase fold and functional diversity. Cell. Mol. Life Sci. 65 (13), 2039–2055. https://doi.org/10.1007/s00018-008-7554-z.

Ehrenhofer-Murray, A.E., 2004. Chromatin dynamics at DNA replication, transcription and repair. Eur. J. Biochem. 271 (12), 2335–2349. https://doi.org/10.1111/j.1432-1033.2004.04162.x.

Franke, D., Petoukhov, M.V., Konarev, P.V., Panjkovich, A., Tuukkanen, A., Mertens, H.D.T., Kikhney, A.G., Hajizadeh, N.R., Franklin, J.M., Jeffries, C.M., Svergun, D.I., 2017. ATSAS: a comprehensive data analysis suite for small-angle scattering from macromolecular solutions. J. Appl. Crystallogr. 50 (Pt 4), 1212–1225. https://doi.org/10.1107/S1600576717007786.

Gao, M., Li, X., Huang, J., Gropp, G.M., Gjetvaj, B., Lindsay, D.L., Wei, S., Coutu, C., Chen, Z., Wan, X.C., Hannoufa, A., Lydiate, D.J., Gruber, M.Y., Chen, Z.J., Hegedus, D.D., 2015. SCARECROW-LIKE15 interacts with HISTONE DEACETYLASE19 and is essential for repressing the seed maturation programme. Nat. Commun. 6, 7243. https://doi.org/10.1038/ncomms8243.

Gu, D., Chen, C.Y., Zhao, M., Zhao, L., Duan, X., Duan, J., Wu, K., Liu, X., 2017. Identification of HDA15-PIF1 as a key repression module directing the transcriptional network of seed germination in the dark. Nucleic Acids Res. 45 (12), 7137–7150. https://doi.org/10.1093/nar/gkx283.

Hao, Y., Wang, H., Qiao, S., Leng, L., Wang, X., 2016. Histone deacetylase HDA6 enhances brassinosteroid signaling by inhibiting the BIN2 kinase. Proc Natl Acad Sci U S A 113 (37), 10418–10423. https://doi.org/10.1073/pnas.1521363113.

Hartl, M., Füßl, M., Boersema, P.J., Jost, J.O., Kramer, K., Bakirbas, A., Sindlinger, J., Plöchinger, M., Leister, D., Uhrig, G., Moorhead, G.B., Cox, J., Salvucci, M.E., Schwarzer, D., Mann, M., Finkemeier, I., 2017. Lysine acetylome profiling uncovers novel histone deacetylase substrate proteins in Arabidopsis. Mol. Syst. Biol. 13 (10), 949. https://doi.org/10.15252/msb.20177819.

Hassig, C.A., Tong, J.K., Fleischer, T.C., Owa, T., Grable, P.G., Ayer, D.E., Schreiber, S.L., 1998. A role for histone deacetylase activity in HDAC1-mediated transcriptional repression. Proc Natl Acad Sci U S A 95 (7), 3519–3524. https://doi.org/10.1073/pnas.95.7.3519.

Hung, F.Y., Chen, F.F., Li, C., Chen, C., Lai, Y.C., Chen, J.H., Cui, Y., Wu, K., 2018. The Arabidopsis LDL1/2-HDA6 histone modification complex is functionally associated with CCA1/LHY in regulation of circadian clock genes. Nucleic Acids Res. 46 (20), 10669–10681. https://doi.org/10.1093/nar/gky749.

Hübner, M.R., Spector, D.L., 2010. Chromatin dynamics. Annu. Rev. Biophys. 39, 471–489. https://doi.org/10.1146/annurev.biophys.093008.131348.

Krämer, O.H., Göttlicher, M., Heinzel, T., 2001. Histone deacetylase as a therapeutic target. Trends Endocrinol. Metab. 12 (7), 294–300. https://doi.org/10.1016/s1043-2760(01)00438-6.

Kim, Y.J., Wang, R., Gao, L., Li, D., Xu, C., Mang, H., Jeon, J., Chen, X., Zhong, X., Kwak, J.M., Mo, B., Xiao, L., Chen, X., 2016. POWERDRESS and HDA9 interact and promote histone H3 deacetylation at specific genomic sites in Arabidopsis. Proc. Natl. Acad. Sci. U.S.A. 113 (51), 14858–14863. https://doi.org/10.1073/pnas.1618618114.

Liu, C., Li, L.C., Chen, W.Q., Chen, X., Xu, Z.H., Bai, S.N., 2013. HDA18 affects cell fate in Arabidopsis root epidermis via histone acetylation at four kinase genes. Plant Cell 25 (1), 257–269. https://doi.org/10.1105/tpc.112.107045.

Lombardi, P.M., Cole, K.E., Dowling, D.P., Christianson, D.W., 2011. Structure, mechanism, and inhibition of histone deacetylases and related metalloenzymes. Curr. Opin. Struct. Biol. 21 (6), 735–743. https://doi.org/10.1016/j.sbi.2011.08.004.

Luger, K., Mäder, A., Sargent, D.F., Richmond, T.J., 2000. The atomic structure of the nucleosome core particle. J. Biomol. Struct. Dyn. 17 (1), 185–188. https://doi.org/10.1080/07391102.2000.10506619.

Luo, M., Tai, R., Yu, C.W., Yang, S., Chen, C.Y., Lin, W.D., Schmidt, W., Wu, K., 2015. Regulation of flowering time by the histone deacetylase HDA5 in Arabidopsis. Plant J. 82 (6), 925–936. https://doi.org/10.1111/tpj.12868.

Luo, M., Wang, Y.Y., Liu, X., Yang, S., Lu, Q., Cui, Y., Wu, K., 2012. HD2C interacts with HDA6 and is involved in ABA and salt stress response in Arabidopsis. J. Exp. Bot. 63 (8), 3297–3306. https://doi.org/10.1093/jxb/ers059.

Ma, X., Lv, S., Zhang, C., Yang, C., 2013. Histone deacetylases and their functions in plants. Plant Cell Rep. 32 (4), 465–478. https://doi.org/10.1007/s00299-013-1393-6.

Millán-Zambrano, G., Burton, A., Bannister, A.J., Schneider, R., 2022. Histone post-translational modifications - cause and consequence of genome function. Nat. Rev. Genet. 23 (9), 563–580. https://doi.org/10.1038/s41576-022-00468-7.

Philo, J.S., 2023. SEDNTERP: a calculation and database utility to aid interpretation of analytical ultracentrifugation and light scattering data. Eur. Biophys. J. 52 (4-5), 233–266. https://doi.org/10.1007/s00249-023-01629-0.

Robert, X., Gouet, P., 2014. Deciphering key features in protein structures with the new ENDscript server. Nucleic Acids Res. 42 https://doi.org/10.1093/nar/gku316 (Web Server issue): W320-4. https://www.ncbi.nlm.nih.gov/pubmed/24753421.

Roth, S.Y., Denu, J.M., Allis, C.D., 2001. Histone acetyltransferases. Annu. Rev. Biochem. 70, 81–120. https://doi.org/10.1146/annurev.biochem.70.1.81.

Schneidman-Duhovny, D., Hammel, M., Tainer, J.A., Sali, A., 2016. FoXS, FoXSDock and MultiFoXS: single-state and multi-state structural modeling of proteins and their complexes based on SAXS profiles. Nucleic Acids Res. 44 (W1), W424–W429. https://doi.org/10.1093/nar/gkw389.

Seto, E., Yoshida, M., 2014. Erasers of histone acetylation: the histone deacetylase enzymes. Cold Spring Harbor Perspect. Biol. 6 (4), a018713 https://doi.org/10.1101/cshperspect.a018713.

Tanaka, M., Kikuchi, A., Kamada, H., 2008. The Arabidopsis histone deacetylases HDA6 and HDA19 contribute to the repression of embryonic properties after germination. Plant Physiol 146 (1), 149–161. https://doi.org/10.1104/pp.107.111674.

Tran, H.T., Nimick, M., Uhrig, R.G., Templeton, G., Morrice, N., Gourlay, R., DeLong, A., Moorhead, G.B., 2012. Arabidopsis thaliana histone deacetylase 14 (HDA14) is an α-tubulin deacetylase that associates with PP2A and enriches in the microtubule fraction with the putative histone acetyltransferase ELP3. Plant J. 71 (2), 263–272. https://doi.org/10.1111/j.1365-313X.2012.04984.x.

Ueda, M., Matsui, A., Tanaka, M., Nakamura, T., Abe, T., Sako, K., Sasaki, T., Kim, J.M., Ito, A., Nishino, N., Shimada, H., Yoshida, M., Seki, M., 2017. The distinct roles of class I and II RPD3-like histone deacetylases in salinity stress response. Plant Physiol 175 (4), 1760–1773. https://doi.org/10.1104/pp.17.01332.

Van Zanten, M., Zöll, C., Wang, Z., Philipp, C., Carles, A., Li, Y., Kornet, N.G., Liu, Y., Soppe, W.J., 2014. HISTONE DEACETYLASE 9 represses seedling traits in Arabidopsis thaliana dry seeds. Plant J. 80 (3), 475–488. https://doi.org/10.1111/tpj.12646.

Vannini, A., Volpari, C., Filocamo, G., Casavola, E.C., Brunetti, M., Renzoni, D., Chakravarty, P., Paolini, C., De Francesco, R., Gallinari, P., Steinkühler, C., Di Marco, S., 2004. Crystal structure of a eukaryotic zinc-dependent histone deacetylase, human HDAC8, complexed with a hydroxamic acid inhibitor. Proc Natl Acad Sci U S A 101 (42), 15064–15069. https://doi.org/10.1073/pnas.0404603101.

Wang, Z., Cao, H., Sun, Y., Li, X., Chen, F., Carles, A., Li, Y., Ding, M., Zhang, C., Deng, X., Soppe, W.J., Liu, Y.X., 2013. Arabidopsis paired amphipathic helix proteins SNL1 and SNL2 redundantly regulate primary seed dormancy via abscisic acid-ethylene antagonism mediated by histone deacetylation. Plant Cell 25 (1), 149–166. https://doi.org/10.1105/tpc.112.108191.

Winn, M.D., Ballard, C.C., Cowtan, K.D., Dodson, E.J., Emsley, P., Evans, P.R., Keegan, R.M., Krissinel, E.B., Leslie, A.G., McCoy, A., McNicholas, S.J., Murshudov, G.N., Pannu, N.S., Potterton, E.A., Powell, H.R., Read, R.J., Vagin, A., Wilson, K.S., 2011. Overview of the CCP4 suite and current developments. Acta Crystallogr D Biol Crystallogr 67 (Pt 4), 235–242. https://doi.org/10.1107/S0907444910045749.

Woodcock, C.L., Ghosh, R.P., 2010. Chromatin higher-order structure and dynamics. Cold Spring Harbor Perspect. Biol. 2 (5), a000596. https://doi.org/10.1101/cshperspect.a000596.

Xu, C.R., Liu, C., Wang, Y.L., Li, L.C., Chen, W.Q., Xu, Z.H., Bai, S.N., 2005. Histone acetylation affects expression of cellular patterning genes in the Arabidopsis root epidermis. Proc Natl Acad Sci U S A 102 (40), 14469–14474. https://doi.org/10.1073/pnas.0503143102.

Yruela, I., Moreno-Yruela, C., Olsen, C.A., 2021. Zn^{+2}-dependent histone deacetylases in plants: structure and evolution. Trends Plant Sci. 26 (7), 741–757. https://doi.org/10.1016/j.tplants.2020.12.011.

Zhao, H., Brautigam, C.A., Ghirlando, R., Schuck, P., 2013. Overview of current methods in sedimentation velocity and sedimentation equilibrium analytical ultracentrifugation. Curr Protoc Protein Sci. https://doi.org/10.1002/0471140864.ps2012s71 (Chapter 20): Unit20.12.

Zheng, Y., Ding, Y., Sun, X., Xie, S., Wang, D., Liu, X., Su, L., Wei, W., Pan, L., Zhou, D.X., 2016. Histone deacetylase HDA9 negatively regulates salt and drought stress responsiveness in Arabidopsis. J. Exp. Bot. 67 (6), 1703–1713. https://doi.org/10.1093/jxb/erv562.

Zhou, J., Wang, X., He, K., Charron, J.B., Elling, A.A., Deng, X.W., 2010. Genome-wide profiling of histone H3 lysine 9 acetylation and dimethylation in Arabidopsis reveals correlation between multiple histone marks and gene expression. Plant Mol. Biol. 72 (6), 585–595. https://doi.org/10.1007/s11103-009-9594-7.